Probing Charged Aqueous Interfaces Near Critical Angles: Effect of Varying Coherence Length

Dennis K. Hore and Eric Tyrode

June 2019

Probing Charged Aqueous Interfaces Near Critical Angles: Effect of Varying Coherence Length

Dennis K. Hore*† and Eric Tyrode*,‡

†*Department of Chemistry, University of Victoria, Victoria, V8W 3V6 Canada*

‡*Department of Chemistry, KTH Royal Institute of Technology, SE-10044 Stockholm, Sweden*

E-mail: dkhore@uvic.ca,tyrode@kth.se

Abstract

Angle-resolved vibrational sum frequency generation experiments have been used to study the silica–water interface as a function of ionic strength. Well below the critical angle, the sum frequency intensity increases up to 10^{-4} M NaCl, and then drops. However, near the critical angle, a plateau may be observed up to 10^{-4} M. We first demonstrate that this is a result of the interaction of a long Debye length at low ionic strength with a long coherence length near the critical angles. In order to account for the behaviour at the lowest concentrations, it is necessary to consider an electrostatic potential that extends into the bulk aqueous phase beyond the Debye-Hückel approximation as a result of the large surface potential. Since the extent of the second- and third-order contributions to the nonlinear polarization can varying with ionic strength, but not with angle of incidence, we perform a global fit to the experimental data using our proposed model to extract the relative magnitude of the two susceptibilities. The ionic strength dependence of this ratio points to the critical nature of the silanol deprotonation and the development of surface charge, and illustrates how the surface water molecules respond. These results highlight the importance of varying the coherence length in order to probe water structure at charged interfaces.

Introduction

Charged aqueous interfaces are of fundamental importance in the environment, and in a host of fundamental and technological applications. The silica–water interface in particular has received much attention due to its natural abundance, and practical use in biotechnology and chemical separations such as liquid chromatography and capillary electrophoresis.[1–5] However, it has also developed into a model system for understanding interfacial water structure in the presence of varying surface charge density as electrolyte ions simultaneously screen the surface charge and promote the development of additional charge.

Of the various methods available for probing charged aqueous interfaces, nonlinear optical techniques such as electronic second-harmonic (SH) and vibrational sum-frequency (SF) generation offer the possibility of *in situ* measurements adjacent to the bulk aqueous phase. These techniques achieve their surface selectivity on account of the symmetry-breaking requirement to produce signal from a second-order polarization $P^{(2)}$ in the electric dipole approximation. Only water molecules in noncentrosymmetric environments can produce a net SH or SF response; signal from bulk water destructively interferes. In the area of surface nonlinear optics,[6] niche application areas have historically been those in which the nonlinear response originates at the interface formed between two centrosymmetric bulk phases. Typically, the distance over which the inversion symmetry is broken and $\chi^{(2)} \neq 0$ is very small (1–2 nm) compared to the nonlinear coherence length (typically tens of nanometers, depending on the geometry). However, at charged surfaces, signal should be generated not only from the proximal interfacial region, but also from water perturbed by the decaying surface electric field.[7–9] In 1992 Eisenthal formulated a model to account for SH observations with varying salt concentration at the silica surface, where a third-order polarization $P^{(3)}$ is introduced resulting from the second-order polarizability of water, the two incoming electric components of the electromagnetic fields, and the surface potential.[7] Since that time, there has been extensive discussion on experimental[9–15] and computational[16–19] approaches to understand the relative contribution of the two sources of nonlinear polarization at charged interfaces in general.

A significant development in the field was the reformulation of Eisenthal's original model to

account for the wavevector mismatch when signals are generated over a region that is sufficiently deep in comparison to the nonlinear coherence length.[20] An important outcome of this model was that the relative contribution of the second- and third-order response functions was dictated not only by the surface potential, but also depends on a screening factor that is a function of both the wavevector mismatch and the Debye length.[8,9] At low ionic strength there is effectively no third-order contribution to the signal as the deeper interfacial layers produce SH or SF that destructively interfere with each other, thereby leaving only the topmost layer second-order response. Likewise, at high ionic strength the Debye length becomes so short that the wavevector mismatch is no longer important, and the third-order response is scaled by the surface potential alone, as in Eisenthal's original proposal. At intermediate ionic strengths, the relative contributions of the wavevector mismatch Δk and Debye length modulate the magnitude and phase of the two response functions.[8,9,21–23]

Although the proposed theory is general, the initial experimental demonstrations have been of the charged air-water interface.[9,13,24] When probing water at charged solid surfaces, it is often desired to have at least one of the incident beams above the critical angle. Although such experiments inherit the burden of careful data treatment to accurately restore the $|\chi^{(2)}|^2$ lineshape from the measured effective susceptibility, the up to three orders of magnitude in signal enhancement[25–27] enables measurement of species such as surface silanols that could not be observed otherwise.[28] In such cases, additional effects of total internal reflection (TIR) need to be considered, as the SF results from generation and excitation from evanescent fields. The role of phase-matching in TIR geometries have been considered extensively in the area of bulk nonlinear optics, as phase matching is a critical consideration in order to build up significant intensity at the frequency of interest. As an alternative to enhanced Δk using techniques such as angle-tuning of birefringent crystals, periodic poling, or from phase shifts incurred in internal reflection,[29–34] TIR has also been considered. Here, although evanescent wave excitation is used, the data may be interpreted based on all nonlinear polarization terms originating sufficiently close to the interface to avoid the explicit consideration of Δk.[35–38]

The importance of the experimental geometry and its implications for controlling Δk may be seen when looking at SF studies of the silica–water interface with varying ionic strength below the critical angle, where an increase in signal with ionic strength initially occurs, followed by a subsequent decrease.[39] This is in sharp contrast to previous results near the critical angle that display a constant SFG intensity up to $\approx$ 1 mM NaCl,[11] before the signal drops. In this work we will demonstrate that such different results are due to the subtle interplay between the wavevector mismatch and the Debye length at angles and concentrations over which both terms compete. We illustrate that restriction of the probed depth under TIR conditions can have dramatic consequences on the measured signals. This not only consolidates new and previous experimental findings, but also provides a new tool for studying charged aqueous interfaces with more facile control of experimental conditions.

Materials and Methods

Materials and sample preparation. Sodium chloride (Puratronic, 99.999% metal basis) from Alfa Aeser was baked before use at 500°C for 90 min to remove potential organic contaminants. The silica substrates consisted of custom-made IR grade fused silica hemispheres of 10 mm in diameter (CVI, Melles-Griot), and windows of 12.7 mm in diameter and 2 mm in thickness (ISP optics). The substrates were cleaned following a procedure that consisted in first sonication in ethanol, followed by rinsing in Milli-Q water, immersion in chromosulphuric acid for 30 min (Merck), and then finally copiously rinsing in Milli-Q water. Substrates were assembled wet in a gas-tight glass measuring cell, which design is described in detail elsewhere.[27] Salt solutions were injected using gas-tight syringes to minimize contact with atmospheric air. The Milli-Q water used in the experiments was obtained from an Integral 15 Millipore filtration unit (18.2 MΩ·cm resistivity, total organic carbon $<$ 3 ppb). All glassware was cleaned with a commercial alkaline agent (Deconex from Borer) and rinsed thoroughly with water.

Sum Frequency spectrometer. The femtosecond SF spectrometer used has been described in

detail elsewhere.[27] Briefly, it consists of a Ti:Sapphire ≈ 90 fs, 1 kHz, ≈ 6 W amplifier (Integra-C, Amplitude Technologies, France), and a HE-TOPAS (Light Conversion, Lithuania) that generates a broadband (≈ 250 cm^{-1}) tunable IR pulse. The main elements of the detection system are an imaging spectrometer (Shamrock SR-303i-B, Andor, Ireland) and an EM-CCD camera (Newton DU971N-UVB, Andor, Ireland). The spectrometer features a large degree of automation, which allows changing in a matter of seconds the angle of incidence (AOI) of the IR and visible beams, as well as the collection optics of the SF beam with an angular precision better than 0.02°. The angular resolution, is however, not limited by the rotational stages, but by the angular spread of the incoming laser beams, which are delivered in a cone of angles that depends on how tightly they are focused. To minimize this effect, the IR and visible beams are loosely focused at the sample position using a +250 mm, and a +1000 mm lens respectively, which correspond to an angle spread of ±0.8° for the IR, and ±0.2° for the visible beam. Spectra were collected on the hemispherical substrates at a fixed IR angle of 55.0°, but variable visible angles: 62.0°, 66.0°, 70.0°, and 74.0°. Due to refraction on the flat window substrates, one additional set of angles was also probed: IR AOI of 35.3° and visible AOI of 40.3°. The non-resonant background from an equivalent gold-coated hemisphere and flat window were used for normalization, following a procedure described in detail elsewhere.[27] The energy of the IR and visible beams were set to ≈ 3 μJ/pulse, and ≈ 7 μJ/pulse, respectively. Measurements were carried out with a spectral resolution of < 2 cm^{-1} and a constant temperature of 22 ± 1°C.

Phase matching in absorbing media and near critical angles

Although the general approach described below is applicable to both second-harmonic and sum-frequency generation, we consider specifically the case of SF generation in what follows: for a visible E_{vis} field incident at ω_{vis} with an angle $\theta_{1,vis}$, and E_{IR} incident at ω_{IR} and an angle $\theta_{1,IR}$, the

signal detected at frequency $\omega_{\mathrm{vis}} + \omega_{\mathrm{IR}}$ is given by

$$I(\omega_{\mathrm{vis}} + \omega_{\mathrm{IR}}) \propto |P^{(2)}(\omega_{\mathrm{vis}} + \omega_{\mathrm{IR}}) + P^{(3)}(\omega_{\mathrm{vis}} + \omega_{\mathrm{IR}})|^2. \tag{1}$$

Additional terms (including $P^{(1)}$, other $P^{(2)}$ and $P^{(3)}$ processes, and higher-order contributions) are excluded since we are assuming that we are able to suitably restrict detection to the frequency $\omega_{\mathrm{vis}} + \omega_{\mathrm{IR}}$, and a relatively small angular range centered around the phase-matching direction. We are therefore interested in those relevant third-order contributions that have the same frequency as the second-order term. The second-order polarization is given by

$$P^{(2)} = \varepsilon_0 E^0_{\mathrm{vis}} E^0_{\mathrm{IR}} \chi^{(2)} \mathrm{e}^{ik_{\mathrm{SF}}z} \tag{2}$$

and the component of the third-order polarization is[8,9]

$$\begin{aligned} P^{(3)} &= \varepsilon_0 \int_0^\infty \chi^{(3)} E_{\mathrm{vis}}(z) E_{\mathrm{IR}}(z) E_0(z) \mathrm{d}z \\ &= \varepsilon_0 \int_0^\infty \chi^{(3)} E^0_{\mathrm{vis}} \mathrm{e}^{ik_{\mathrm{vis}}z} E^0_{\mathrm{IR}} \mathrm{e}^{ik_{\mathrm{IR}}z} E_0(z) \mathrm{d}z \\ &= \varepsilon_0 E^0_{\mathrm{vis}} E^0_{\mathrm{IR}} \left[\int_0^\infty \chi^{(3)} E_0(z) \mathrm{e}^{i\Delta k z} \mathrm{d}z \right] \mathrm{e}^{ik_{\mathrm{SF}}z} \end{aligned} \tag{3}$$

where the wavevector mismatch in the z direction, along the surface normal (using the convention where the magnitude of the z-component is implied[40]) is given by

$$\Delta k = |k_{\mathrm{vis},z} + k_{\mathrm{IR},z} - k_{\mathrm{SF},z}|, \tag{4}$$

with

$$k_{i,z} = \left(\frac{2\pi N_{2,i}}{\lambda_{\mathrm{i}}} \right) \cos \theta_{2,i} \tag{5}$$

where N_2 is the complex-valued refractive index of medium 2 (aqueous solution), λ is the wavelength in vacuum, and θ_2 is the complex-valued refracted angle. In the following, we will neglect the phase factor $\mathrm{e}^{ik_{\mathrm{SF}}z}$ common to the $P^{(2)}$ and $P^{(3)}$ terms, as this will not appear in the intensity

in Eq. 1. Above the critical angle, the aqueous phase is probed with an evanescent field that decays exponentially with an attenuation constant that depends on the refractive indices of the adjacent bulk phases, the angle of incidence, and the wavelength of the probing field. Further, if the lower index medium is absorbing, there is an additional attenuation due to the field extinction coefficient. All of these effects can be taken into consideration with a complex-valued wavevector $k = \mathbb{R}\mathrm{e}\{k\} + i\,\mathbb{I}\mathrm{m}\{k\}$ in the expression for Δk. Fig. 1a illustrates the SF phase mismatch along z, plotted in the complex plane for the case of transparent phases below the critical angle. Since the wavevectors are all real, they lie perfectly along the horizontal axis, and the resultant Δk has its maximum value. Correspondingly, the nonlinear coherence length $\ell_c = 2\pi/\Delta k$ has its minimum value (Fig. 2a). Below the critical angle, but now considering the IR beam is absorbed in the aqueous phase, the refracted angle θ_2 and therefore the z-component of the IR wavevector becomes complex, as shown in Fig. 1b. Above the visible beam critical angle, its wavevector shrinks and rotates by 90° (Fig. 1c). When both visible and SF beams are above the critical angle, Δk has its smallest value (Fig. 1d) and $\ell_c > 1$ μm (Fig. 2a).

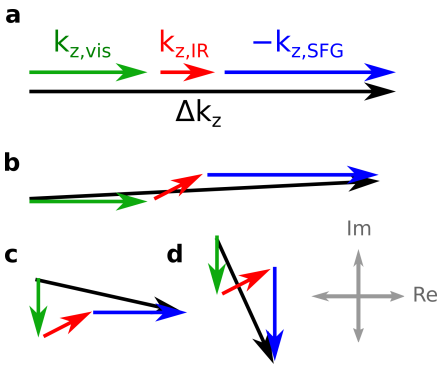

Figure 1: Wavevector mismatch along the surface normal, plotted in the complex plane for (a) transparent phases below the critical angle, (b) below the critical angle, but for IR absorption, (c) above the visible critical angle, (d) above the visible and SF critical angles.

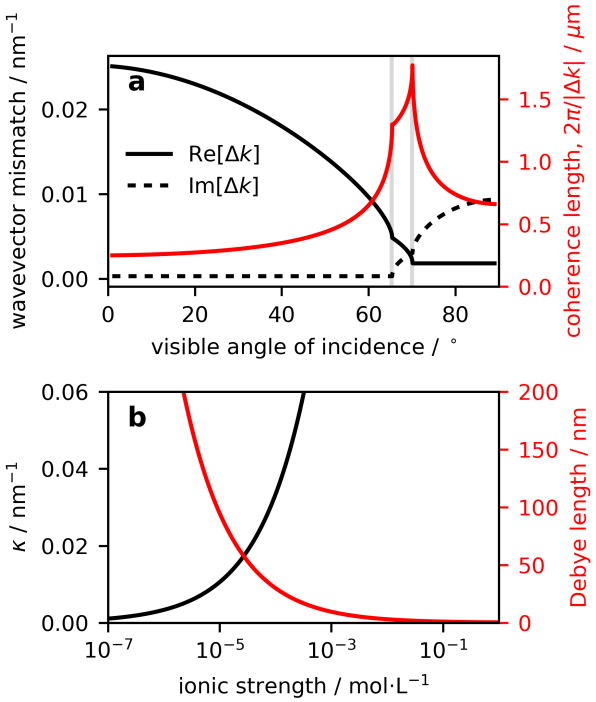

Figure 2: (a) The complex-valued wavevector mismatch along z, Δk (real in solid black lines, imaginary in dashed black lines), along with the coherence length $\ell_c = 2\pi/|\Delta k|$ (red), as a function of the visible beam angle of incidence. The incoming IR beam is fixed at 55°. (b) The Debye length plotted in red, and its reciprocal κ in black.

Electrostatic potential

Distance-dependence of the potential

When the surface electrostatic field E_0 and Δk are the only z-dependent terms, the integral in Eq. 3 may be written to obtain

$$P^{(3)} = \varepsilon_0 \chi^{(3)} E^0_{\text{vis}} E^0_{\text{IR}} \left[\Phi_0 + i\Delta k \int_0^\infty \Phi(z) \mathrm{e}^{i\Delta k z} \mathrm{d}z \right] \tag{6}$$

where the surface potential $\Phi_0 \equiv \Phi(z = 0)$. To solve the integral, a functional form for the electrostatic potential as a function of distance from the surface is required. For relatively low surface potentials (less than ≈ 25 mV) the solution from the linearized Gouy Chapman model can be assumed $\Phi(z) = \Phi_0 \mathrm{e}^{-\kappa z}$ (where κ is the reciprocal Debye length) and further simplification is

possible, resulting in

$$\begin{aligned} P^{(3)} &= \varepsilon_0 \chi^{(3)} E^0_{\text{vis}} E^0_{\text{IR}} \Phi_0 \left[\frac{\kappa}{\kappa - i\Delta k} \right] \\ &= \varepsilon_0 \chi^{(3)} E^0_{\text{vis}} E^0_{\text{IR}} \Phi_0 f_3, \end{aligned} \tag{7}$$

keeping with the f_3 notation from Ref. 8. However, for larger potentials the full solution for $\Phi(z)$ from the Poisson-Boltzmann equation in the Gouy Chapman theory is more appropriate,

$$\begin{aligned} \Phi(z) &= \frac{2kT}{e} \ln \left[\frac{1 + \xi \mathrm{e}^{-\kappa z}}{1 - \xi \mathrm{e}^{-\kappa z}} \right] \\ &= \frac{4kT}{e} \sum_{n=1}^{\infty} \frac{(\xi \mathrm{e}^{-\kappa z})^{2n-1}}{2n-1} \\ &= \frac{4kT}{e} \left[\xi \mathrm{e}^{-\kappa z} + \frac{\xi^3 \mathrm{e}^{-3\kappa z}}{3} + \frac{\xi^5 \mathrm{e}^{-5\kappa z}}{5} + \frac{\xi^7 \mathrm{e}^{-7\kappa z}}{7} + \cdots \right] \end{aligned} \tag{8}$$

where

$$\xi = \tanh \left[\frac{e\Phi_0}{4kT} \right],$$

e is the electron charge, k is Boltzmann's constant, and T is the absolute temperature. In such case, the integral in Eq. 6 either needs to be solved numerically, or using the series expansion with sufficiently large n to assure convergence. The series lends itself well to integration such that

$$\begin{aligned} &\int_0^{\infty} \Phi(z) \mathrm{e}^{i\Delta k z} \mathrm{d}z \\ &= \frac{4kT}{e} \int_0^{\infty} \left[\mathrm{e}^{i\Delta k z} \sum_{n=1}^{\infty} \frac{(\xi \mathrm{e}^{-\kappa z})^{2n-1}}{2n-1} \right] \mathrm{d}z \\ &= -\frac{4kT}{e} \sum_{n=1}^{\infty} \frac{\xi^{2n-1}}{(2n-1)[i\Delta k - \kappa(2n-1)]}. \end{aligned} \tag{9}$$

This ultimately results in the expression for the third-order polarizability

$$\begin{aligned} P^{(3)} &= \varepsilon_0 \chi^{(3)} E^0_{\text{vis}} E^0_{\text{IR}} \left[\Phi_0 - \frac{4ikT\Delta k}{e} \sum_{n=1}^{\infty} \frac{\xi^{2n-1}}{(2n-1)[i\Delta k - \kappa(2n-1)]} \right] \\ &= \varepsilon_0 \chi^{(3)} E^0_{\text{vis}} E^0_{\text{IR}} g_3. \end{aligned} \tag{10}$$

Comparing this expression with Eq. 7, we note that we can no longer factor out the surface potential from g_3. However, if we consider that $g_3 = \Phi_0 - g_3'$, it is consistent with the previous result in that $g_3' \rightarrow 0$ at high ionic strength, providing the same result as $f_3 \rightarrow 1$ in that the full surface potential participates in the interference of the $\chi^{(2)}$ and $\chi^{(3)}$ terms.

Surface potential

The key expressions we have introduced involve the surface potential. Before we can describe the experimental data, we therefore need a formalism for evaluating Φ_0. We employ the same approach that has been successfully used to model the deprotonation of surface carboxylic acid groups as a function of salt concentration.[24] The charge on the silica surface results from the dissociation of silanol groups, which can be represented by the reaction $SiOH \rightleftharpoons H^+ + SiO^-$ and dissociation constant (K_a). Although silica surfaces have been proposed to have different types of silanols with corresponding pK_as,[7,28,41–43] given that measurements were carried out at pH 6, we assume a single equilibrium constant

$$K_a = \frac{[H^+]_0[SiO^-]_0}{[SiOH]_0} \tag{11}$$

where the surface proton concentration $[H^+]_0$ can be expressed in terms of that in the bulk $[H^+]_\infty$ by

$$[H^+]_0 = [H^+]_\infty \exp\left[-\frac{e\Phi_0}{kT}\right]. \tag{12}$$

This enables us to write the equilibrium constant in terms of the fraction of the surface that is deprotonated, α

$$K_a = \frac{\alpha}{1-\alpha}[H^+]_\infty \exp\left[-\frac{e\Phi_0}{kT}\right]. \tag{13}$$

The surface potential also depends on the area per silanol A_M through the surface charge density $\sigma = \alpha e / A_M$ as described by the Grahame equation

$$\Phi_0 = \frac{2kT}{e} \sinh^{-1}\left[\frac{\alpha e}{A_M\sqrt{8I\varepsilon\varepsilon_0 kT}}\right] \tag{14}$$

Introducing Eq. 14 into Eq. 13, results in an expression that relates the degree of deprotonation to the ion concentration in solution, which can then be used to calculate the surface potential.

$$\sqrt{I} = \frac{\alpha e}{A_{\mathrm{M}}\sqrt{8\varepsilon\varepsilon_0 kT}}\left[\sinh\left(\frac{1}{2}\left(\ln[\mathrm{H}^+]_\infty - \ln K_a - \ln\left(\frac{1-\alpha}{\alpha}\right)\right)\right)\right]^{-1} \tag{15}$$

We have considered an area per silanol group of $A_M = 200$ Å^2 and p$K_a = 4$ in order to determine the deprotated fraction α and the corresponding surface charge density $\sigma = \alpha e/A_{\mathrm{M}}$ (see justification in the Supporting Information). The variation of the surface charge with ionic strength is plotted in Fig. 3a, and the resulting surface potentials and surface hydronium concentrations are plotted in Fig. 3b and 3c, respectively.

Contribution of $\chi^{(3)}$ and Φ_0 at low ionic strengths near the critical angle

As shown in Eq. 10, the g_3 factor is entirely responsible for the nature of the interference between $\chi^{(2)}$ and $\chi^{(3)}$ contributions to the SF signal, and depends on the angle of incidence, the ionic strength, and the surface potential (itself a function of ionic strength). With our model for Φ_0 in place, we are now in a position to explore the concentration and angle dependence of g_3. As g_3 is a complex quantity, we plot the magnitude $|g_3|$ in Fig. 4a, and phase ϕ_g in Fig. 4b.

A general trend may be observed where $|g_3|$ first increases and then decreases with increasing ionic strength. However, the extent to which $|g_3|$ rises from 10^{-7}–10^{-4} M is more pronounced at lower angles of incidence. The features are somewhat suppressed near the visible and SF critical angles. Note that these features are present in g_3 itself, independent of any local field effects that may contribute to signal enhancement near the critical angle. Now studying the phase of g_3, we notice that, in the vicinity of the critical angles, $\phi_g \rightarrow 180°$. In other words, g_3 is nearly real and negative above approximately 70°. The interesting behaviour at low ionic strengths and near the critical angles is due to the comparable magnitudes of κ and Δk in this region, as shown in Fig. 2.

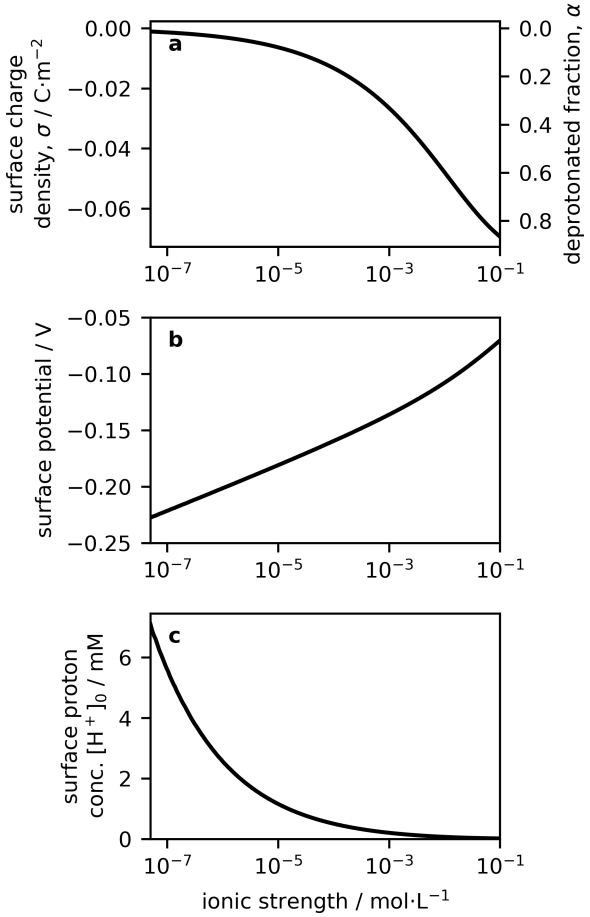

Figure 3: (a) The fraction of silica surfaces sites deprotonated as a function of ionic strength, and the corresponding net surface charge density. (b) The resulting surface potential and (c) the surface hydronium ion concentration as a function of ionic strength.

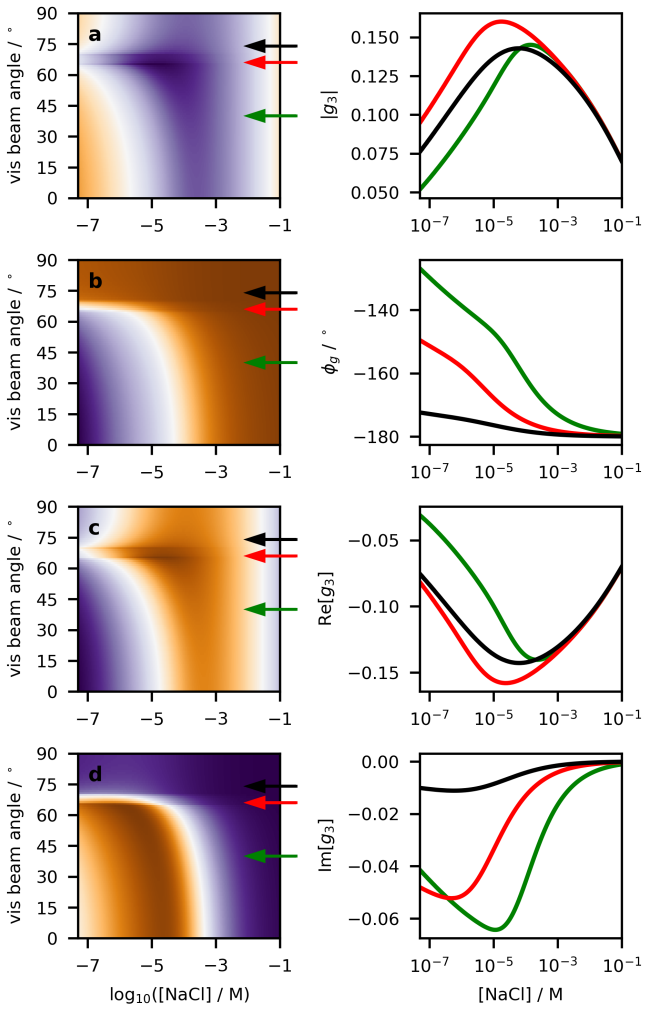

Figure 4: Values of the (a) magnitude, (b) phase, (c) real and (d) imaginary components of g_3 as a function of the ionic strength and angle of incidence of the visible beam. In all cases the incoming IR beam was fixed at 50°. A slice through the 40° incident visible angle is shown in green, 66° in red, and 74° in black. Numerical values corresponding to the minimum (darkest orange) and maximum (darkest purple) colors are the same as the extent of the axes in the corresponding plots with the slices in the right column.

Further comparison between g_3 and the f_3 factor previously described from the linearized Gouy Chapman model may be found in Fig. S3 and S4.

Experimental results

To evaluate the influence of the experimental geometry on the dependence of the SF intensity with ionic strength, spectra were collected at various angles of incidence. SF spectra at the fused silica–electrolyte interface for two selected angular combinations, corresponding to conditions above and below the visible and SF critical angles, are shown in Figs. 5a and 5b (equivalent spectra for the three additional experimental geometries can be found in the ¨Figs. S5, S6 and S7). The spectra in the OH stretching region show contributions from surface silanol groups and water molecules in direct proximity to the interface (contributing to $\chi^{(2)}$), as well as those further into the bulk in the diffuse double layer perturbed by the surface electric field (contributing to $\chi^{(3)}$). Three distinct relative broad bands centred at $\approx 3200\ \mathrm{cm}^{-1}$, $\approx 3400\ \mathrm{cm}^{-1}$ and $\approx 3660\ \mathrm{cm}^{-1}$ can be resolved in the ssp polarization spectra shown in Fig. 5. Although the precise assignments of the first two bands remains controversial,[44–48] at the low ionic strengths considered here, they are primarily linked to water molecules in the diffuse double layer. In contrast, the third band at higher frequencies, assigned to the Si-OH stretch of hydrated isolated silanols,[28] or possibly H_2O molecules interacting with siloxane groups,[49] originates from the immediate surface.

When changing the ionic strength of the solution the overall SF intensity varies substantially (Fig. 5a and 5b). However, the trends differ depending on the visible AOI. At 62°, silica in contact with pure water shows medium intensity, reaches a maximum at $\approx$ 100 μM NaCl, and decreases thereafter. At 70° AOI, when the nonlinear coherence length is the longest (Fig. 2a), the intensity is already maximum for pure water and remains largely constant, decreasing only at NaCl concentrations higher than $\approx$ 100 μM. The spectral shape also shows variations between the two experimental geometries. This is partly due to local field factors that, in addition to drastically enhancing the overall SF intensity (notice the higher signal to noise of the 70° compared to the 62°

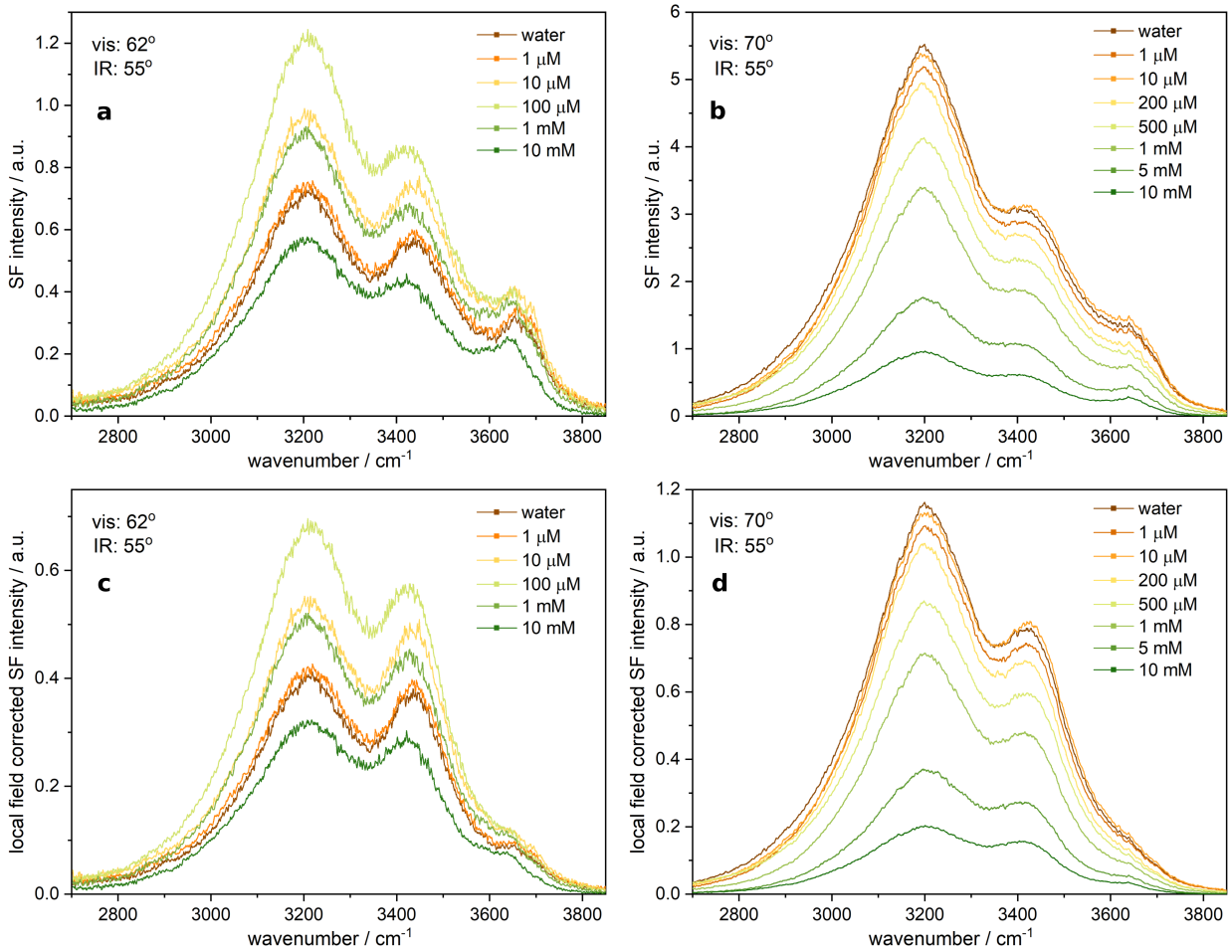

Figure 5: Top row: SF intensity spectra collected in the ssp polarization combination as a function of NaCl concentration for a constant IR angle of incidence of 55° and a 800 nm beam incident at (a) 62° and (b) 70°. Bottom row: the same spectra after correcting for the frequency-dependent local field factors at (c) 62° and (d) 70°.

spectra), show a pronounced frequency dependence close to the critical angles.[27] The influence of these local field factors (L_{ii}) can be removed from the spectra. Combining Eqs. 1 and 10, we can write an expression for the SF intensity

$$\begin{aligned} I_{\text{ssp}} &\propto |\chi^{(2)}_{\text{eff,ssp}} + g_3\chi^{(3)}_{\text{eff,ssp}}|^2 \\ &= |L_{yy}L_{yy}L_{zz}\chi^{(2)}_{yyz} + L_{yy}L_{yy}L_{zz}L^{z=0}_{zz}g_3\chi^{(3)}_{yyzz}|^2 \\ &= |L_{yy}L_{yy}L_{zz}|^2|\chi^{(2)}_{yyz} + g_3\chi^{(3)}_{yyzz}|^2 \end{aligned} \tag{16}$$

since $L^{z=0}_{zz} = 1$. The experimental data can then be corrected for any surface field enhancements using the wavelength dependent refractive indices for fused silica and water to obtain L_{ii} for the SF, visible, and infrared beams (see Supporting Information for details). The corrected spectra after consideration of the local field corrections are shown in Fig. 5c and 5d. This is an important step in the data treatment, as we remove any angle-dependent contributions from L_{ii}, thereby revealing the angle-dependence of the underlying g_3 as shown in Fig. 4.

Although the spectral shape for the two experimental geometries becomes much more similar after correction for the local field factors, subtle differences remain apparent, particularly at low ionic strengths (Fig. 5c and 5d). At 70° and concentrations below 100 μM, we preferentially probe water in the diffuse double layer, as both the Debye screening and nonlinear coherent lengths are long. This situation is to some extent also encountered in the 62° spectra at intermediate concentrations (i.e. 100 μM). In such cases, and similar to other negatively charged interfaces,[9,24] the homodyne SF spectra is characterized by a strong $\approx$ 3200 cm^{-1} band and a slightly weaker intensity at $\approx$ 3400 cm^{-1}. In contrast, contributions from the immediate surface become apparent when the signal from water molecules in the diffuse double layer is reduced. This comes about by shortening the Debye screening length at higher ionic strengths (i.e. 10 mM NaCl), or equivalently, by probing low ionic strengths with short coherence lengths (i.e. 40° or 62°), as the signal from the diffuse double layer partially cancels due to destructive interference. The feature at $\approx$ 3660 cm^{-1} from isolated hydrated silanols then becomes better resolved, and the relative intensity of the $\approx$ 3400 cm^{-1} band is also seen to increase, suggesting that either water molecules directly interacting

with surface and/or other types of hydrated silanol groups (i.e. vicinal, geminal, or hydrogen bonded[1,28,50]) contribute to the band envelope. These differences are more effectively visualized in the normalized spectra presented in Fig. 6.

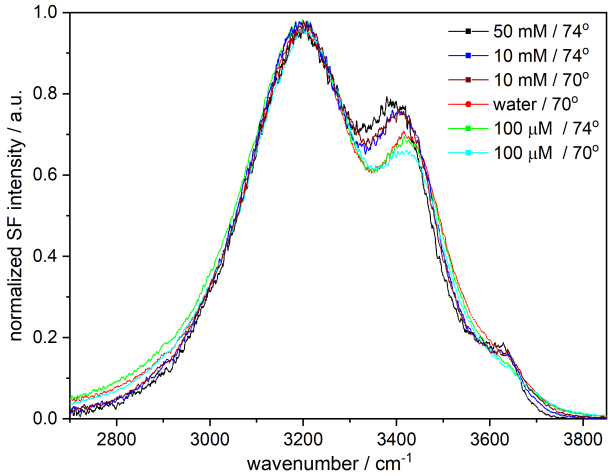

Figure 6: Normalized local field corrected SF intensity at different experimental geometries and ionic strengths, highlighting the spectral differences when contributions from water molecules in the diffuse double layer are reduced upon increasing the ionic strength (see text for details).

To facilitate the comparison between the measured experimental response with the proposed g_3 model, we integrate the local field corrected spectra to obtain what we refer to as corrected SF intensity

$$I_c = \int_{2800}^{3800} \frac{I_{\mathrm{ssp}}}{|L_{yy} L_{yy} L_{zz}|^2} \mathrm{d}\omega. \tag{17}$$

which after applying a normalization procedure (Fig. S9, and described in the Supporting Information), leads to the data depicted in Fig. 7, which summarizes all experimental results. Fig. 7 highlights the importance of the experimental geometry and resolves the apparent discrepancies observed in previous SF studies at the silica-electrolyte interface at angles below[39] and in close proximity to the critical angle.[11,28] It also provides the opportunity to test our g_3 model and determine the relative magnitude of $\chi^{(2)}$ and $\chi^{(3)}$, as the ratio for a given ionic strength should be equivalent for all angles of incidence.

We first re-write Eq. 17 in a manner that explicitly reveals the magnitude and phase of the

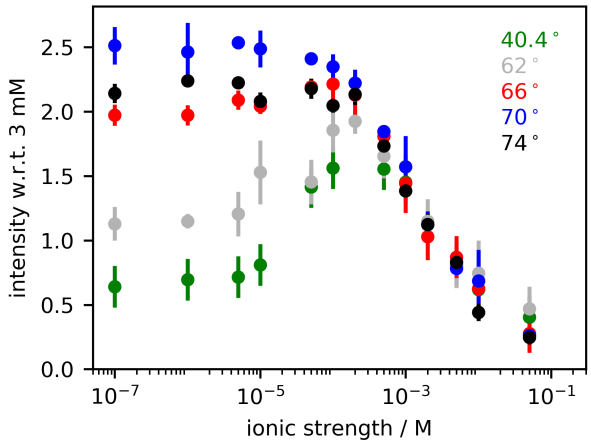

Figure 7: The local field-corrected integrated spectral intensity as a function of ionic strength and angle of incidence, normalized to the projected intensity at 3 mM. Errors bars represent one standard deviation of the mean obtained from replicate measurements

complex quantities

$$\begin{aligned} I_c &\propto \left| |\chi^{(2)}| e^{i\phi_2} + |g_3| e^{i\phi_g} |\chi^{(3)}| e^{i\phi_3} \right|^2 \\ &= |\chi^{(2)}|^2 + |g_3 \chi^{(3)}|^2 + 2|g_3 \chi^{(2)} \chi^{(3)}| \cos(\phi_2 - \phi_3 - \phi_g) \end{aligned} \tag{18}$$

where $\chi^{(2)} = |\chi^{(2)}| e^{i\phi_2}$ and $\chi^{(3)} = |\chi^{(2)}| e^{i\phi_3}$. We then introduce $I' = I_c / |\chi^{(3)}|^2$ to obtain

$$I' \propto \left| \frac{\chi^{(2)}}{\chi^{(3)}} \right|^2 + |g_3|^2 + 2|g_3| \left| \frac{\chi^{(2)}}{\chi^{(3)}} \right| \cos(\phi_2 - \phi_3 - \phi_g) \tag{19}$$

and let $R \equiv |\chi^{(2)}| / |\chi^{(3)}|$ and $\Delta\phi \equiv \phi_2 - \phi_3$ to arrive at

$$I' \propto R^2 + |g_3|^2 + 2R|g_3| \cos(\Delta\phi - \phi_g). \tag{20}$$

Eq. 20 has only two unknown parameters, R and $\Delta\phi$. Results from a recent theoretical study have shown that below 100 mM, $\chi^{(3)}$ is essentially independent of ionic strength.[17] We therefore interpret any salt concentration dependence of R as a variation in $\chi^{(2)}$ due to reorientation of surface water molecules and/or silanol groups as a result of a salt induced deprotonation of the surface.

We have explored the effect of $\Delta\phi$ in accounting for the shape of the experimental data, and

observed that it is largely insensitive to the values of $\Delta\phi$, as long as they are set to $180° \pm 20°$ (see Figs. S10–S12 for support). The data for all experimental geometries in Fig. 7 are then globally fit to Eq. 20, having R as the only unknown parameter. The best fits for R as a function of ionic strength, and corresponding angular-dependent SF intensities are shown as open circles in Fig. 8a and c, respectively. By employing an empirical function that fits the general trend observed for R (continuous solid line in Fig. 8a), the intensity predicted for any angle of incidence and ionic strength in the range 10^{-7}–0.1 M can be visualized in Fig. 8b (black squares indicate points corresponding to the experimental measurements). Slices of this 2D profile taken at the experimental angles of incidence are plotted as lines in Fig. 8c, which are seen to follow the general experimental trends. Several interesting points can be extracted from Fig. 8. At low ionic strengths, molecules in the diffuse double layers are preferentially probed near the critical angles. This is a consequence of the longer nonlinear coherence lengths, which limit the the signal cancellation due to interference (see Fig. 8b). Second, $\chi^{(2)}$ contributions from molecules in the proximal interfacial region decrease non-monotonically with ionic strength, and this is largely irrespective of the values chosen for the pK_a and silanol A_{M} used in estimating the surface potential.

Discussion

Relative contribution of $\chi^{(2)}$ and $\chi^{(3)}$ as a function of ionic strength. In order to reproduce the trends in the different experimental geometries, our model indicates that the ratio of $\chi^{(2)}$ over $\chi^{(3)}$ decreases non-monotonically with ionic strength (Fig. 8a). The potential origin of this behavior is discussed in what follows. Given that the absolute value of $\chi^{(3)}$ has been experimental shown[9] and theoretically calculated[17] to be constant for the low ionic strength considered here, the direct implication is that the SF response from molecules in the immediate interface (i.e. $\chi^{(2)}$) decreases upon addition of salt. A lower response can come about by a decreasing number of contributing OH oscillators, orientational broadening, and/or an increase of oscillators with opposite or unfavorable orientations. Since the OH stretching region is specifically targeted through

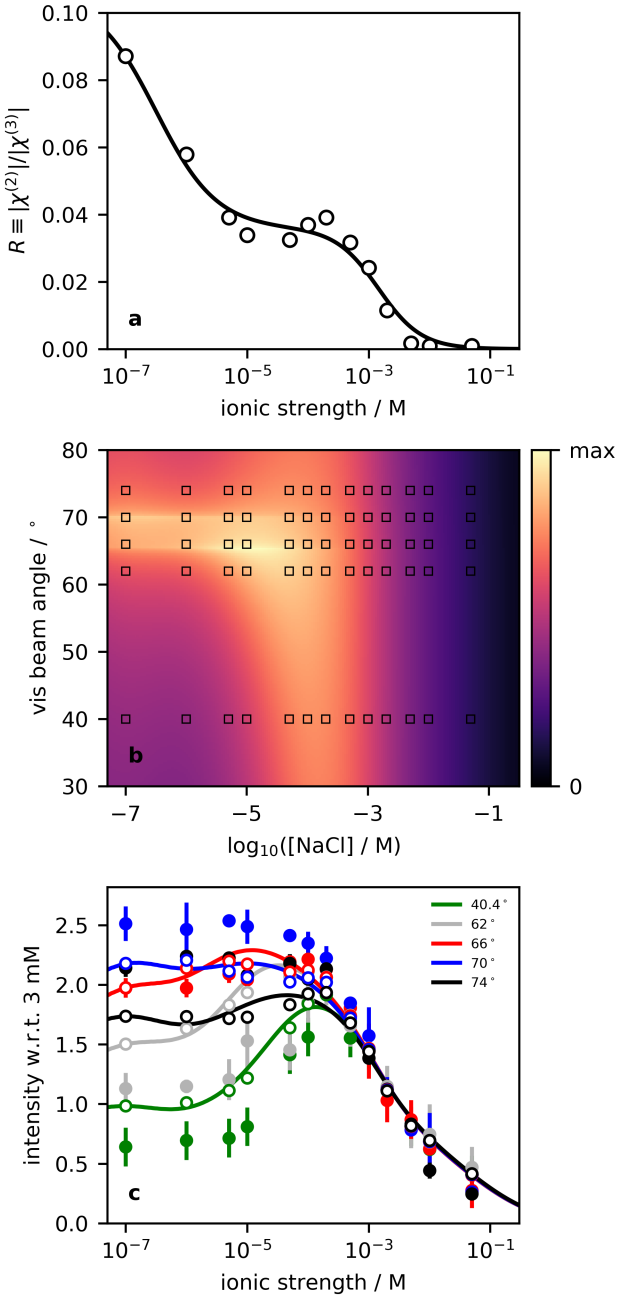

Figure 8: (a) Results from a global fit to the experimental data across all angles and concentrations in order to obtain the $|\chi^{(2)}/\chi^{(3)}|$ ratio R (points), along with an empirical trend line (solid line). (b) The predicted SF intensity as a function of the visible beam angle of incidence and ionic strength, based on the trend line in the previous panel. Points at which experimental measurements were performed are indicated with black squares. (c) Angle slices through the 2D map illustrating the ionic strength dependence (lines), superimposed on the experimental data (solid points) and the value of fit to obtain R without interpolation (open circles).

the vibrational resonance, both H_2O and Si-OH groups are expected to contribute. Starting from pure water, the surface charge density increases almost two orders of magnitude upon the addition of salt in the concentration range of interest (see Fig. 3a). As the surface charge stems from the deprotonation of silanols groups, the immediate consequence is that their number must decrease accordingly. In contrast, the total number of water molecules at the interface is not expected to change significantly. However, their average polar orientation will change gradually as the surface becomes more negatively charged. There will be a transition from having the hydrogen atoms pointing away from the surface (accepting hydrogen bonds from silanol groups), to having them facing the surface and the SiO^- silanolate groups.[46]

The reduced number of silanols and the partial flip of water molecules at the surface would explain the observed decrease in R with ionic strength. Nonetheless, two features grant further consideration. First, the apparent plateau in R values at intermediate salt concentrations, and second, the fact that R decreases to almost zero at 10 mM NaCl. The former can be addressed by recalling that the hydronium ion concentration at the surface is several orders of magnitude higher than in the bulk (Fig. 3c). This is a consequence of the negative surface potential, which is highest for pure water. The surface hydronium ion concentration is then $\approx$ 6 mM in water, and decreases to sub-mM concentrations when the ionic strength is higher than 10^{-5} M. The implication is that in pure water almost all surface silanols ($pK_a \approx 4$) are found in their protonated form, and are roughly 50% deprotonated when the surface proton concentration is $\approx$ 0.1 mM, which happens close to the middle of the plateau region. Thereby, the apparent plateau of the R value could be linked to the titration of the SiOH groups.

Although the number of protonated silanol groups reduces at 10 mM, the fraction of dissociated silanol never exceeds 20%.[51] The near-zero value of R at 10 mM must therefore be associated with signal cancellation due to destructive interference, with OH groups adopting opposite orientations. Consequently, OH groups from silanols should continue to contribute to the $\chi^{(2)}$ response. In fact the SF spectra supports this conclusion as the band at $\approx$ 3660 cm^{-1} linked to surface silanols remains clearly visible at the highest salt concentrations measured. The cancellation of the signal

will then originate from populations of water molecules displaying opposite orientation, hydrating the remaining silanol groups, or interacting with the charged silanolates. The implication is that R value is expected to increase at concentrations higher than those measured here.

Comparison with heterodyne measurements in the literature. One of the advantages of heterodyne-detected SF experiments is that measurement of the phase enables the spectrum of $\mathbb{I}\mathrm{m}\{\chi^{(2)}\}$ to be obtained, rather than $|\chi^{(2)}|$ or $|\chi^{(2)}|^2$. This is especially important as $\mathbb{I}\mathrm{m}\{\chi^{(2)}\}$ reveals more subtle features that could otherwise be obscured in the intensity spectrum. Heterodyne measurements at buried interfaces[46,48] remain a technical challenge, especially for water, where the choice of phase reference is critical. A recent heterodyne measurement of the silica-water interface at pH 12 with varying NaCl concentration revealed that the shape of the spectra was unchanged up to $\approx$ 1 M.[48] Most important, $\mathbb{I}\mathrm{m}\{\chi^{(2)}\} > 0$ over the entire O–H stretching region in this concentration range. We can gain some insight into our result by assuming that the $\chi^{(3)}$ spectrum of any dilute aqueous interface should be the same. In other words, water near the surface may exhibit a different $\chi^{(2)}$ spectrum according to the nature of the surface, but diffuse layer water aligned by the electric field is independent of the nature of the surface. Following this assumption, we can use the $\mathbb{I}\mathrm{m}\{\chi^{(3)}\}$ component extracted for the charged air–water interface by Wen *et al.*[9] That study showed that, for a net negatively-charged surface, $\mathbb{I}\mathrm{m}\{\chi^{(3)}\} < 0$ over the entire O–H region. First, this provides further evidence for our conclusion that $\Delta\phi \approx 180°$. Close inspection of the $\mathbb{I}\mathrm{m}\{\chi^{(2)}\}$ spectra from Ref. 48 and the $\mathbb{I}\mathrm{m}\{\chi^{(3)}\}$ spectra from Ref. 9 shows that, with the exception of the opposite signs, the shape of the two spectra are very similar. This further supports our conclusion that $\Delta\phi$ should be close to 180°.

We can also use the above literature results to comment on the spectral shape of the response at ionic strength below 10 mM. If we define the measured signal as $\mathbb{I}\mathrm{m}\{S\}$, we can write the heterodyne version of Eq. 19 as

$$\begin{aligned}\mathbb{I}\mathrm{m}\{S\} &= \mathbb{I}\mathrm{m}\{\chi^{(2)} + g_3\chi^{(3)}\} \\ &= \mathbb{I}\mathrm{m}\{\chi^{(2)}\} + \mathbb{R}\mathrm{e}\{g_3\}\,\mathbb{I}\mathrm{m}\{\chi^{(3)}\} + \mathbb{R}\mathrm{e}\{\chi^{(3)}\}\,\mathbb{I}\mathrm{m}\{g_3\}.\end{aligned} \tag{21}$$

At high ionic strength, $\mathbb{R}\mathrm{e}\{g_3\} \rightarrow \Phi_0$ and $\mathbb{I}\mathrm{m}\{g_3\} \rightarrow 0$ as shown in Fig. 4c and d. This reduces Eq. 21 to $\mathbb{I}\mathrm{m}\{S\} = \mathbb{I}\mathrm{m}\{\chi^{(2)}\} + \Phi_0\,\mathbb{I}\mathrm{m}\{\chi^{(3)}\}$. We also consider the limiting case of infinite dilution, where Fig. 4c and 4d show that $\mathbb{R}\mathrm{e}\{g_3\} = \mathbb{I}\mathrm{m}\{g_3\} \rightarrow 0$ and so $\mathbb{I}\mathrm{m}\{S\} \rightarrow \mathbb{I}\mathrm{m}\{\chi^{(2)}\}$ as we expect. Note that, in the g_3 model, this is realized at unphysically low concentrations (below 10^{-10} M, see Fig. S2). We can then predict how complex-valued g_3 might contribute to the spectra at intermediate ionic strengths by incorporating some of the dispersive $\mathbb{R}\mathrm{e}\{\chi^{(3)}\}$ into the lineshape.

Conclusions

We have illustrated that, when using nonlinear optical probes to study charged aqueous interfaces, the information that can be obtained is greatly enhanced by working in an internal reflection geometry near the critical angles. This is a result of the boost in coherence length, combined with the commensurate Debye length, that makes the experimental system especially sensitive to relative contributions of surface- and field-induced susceptibilities. Exploiting the sensitivity of such regimes, we have observed that $\chi^{(2)}$ accounts for nearly 10% of the SFG signal at 10^{-7} M, but rapidly drops as the ionic strength increases, to the point where there is no significant $\chi^{(2)}$ contribution above 10 mM salt. As we still observe silanol signals at these high contributions, we proposed that signal cancellation from ordered species must be responsible, rather than a disordered interfacial environment. Working in such geometries and considering the varying coherence length opens up possibilities for studying charged aqueous interfaces with enhanced structural interpretation.

Acknowledgement

DKH acknowledges support from the Natural Science and Engineering Research Council of Canada and the Canadian Foundation for Innovation. ET has received support from the Swedish Research Council (VR) and the Swedish Foundation for Strategic Research (SSF, FFL-5 program). We thank Laetitia Dalstein for performing some of the preliminary experiments. Fitting experimental data

was performed using WestGrid and Compute Canada resources; we thank Belaid Moa (University of Victoria, WestGrid, Compute Canada) for assistance with resource allocation. We are grateful to Prof. Robert Boyd (University of Ottawa, University of Rochester) for discussion on the topic of phase matching in absorbing media.

Supporting Information Available

Model of distance-dependent potential; f_3 and $\Phi_0 \cdot f_3$ as function of incident beam angle and ionic strength; local field correction to experimental spectra; normalization of experimental data; evaluating the relative phase between $\chi^{(2)}$ and $\chi^{(3)}$.

References

(1) Iler, R. K. *The Chemistry of Silica: Solubility, Polymerization, Colloid and Surface Properties, and Biochemistry*; Wiley: New York, 1979.

(2) Rimola, A.; Costa, D.; Sodupe, M.; Lambert, J.-F.; Ugliengo, P. Silica Surface Features and Their Role in the Adsorption of Biomolecules: Computational Modeling and Experiments. *Chem. Rev.* **2013**, *113*, 4216–4313.

(3) Bergna, H. E.; Roberts, W. O. *Colloidal Silica: Fundamentals and Applications*; Taylor & Francis: New York, 2005.

(4) Papirer, E. *Adsorption on Silica Surfaces*; Marcel Dekker: New York, 2000.

(5) Tan, W.; Wang, K.; He, X.; Zhao, X. J.; Drake, T.; Wang, L.; Bagwe, R. P. Bionanotechnology Based on Silica Nanoparticles. *Med. Res. Rev.* **2004**, *24*, 621–638.

(6) Shen, Y. Surface Nonlinear Optics: A Historical Perspective. *IEEE J. Sel. Top. Quan. Elec.* **2000**, *6*, 1375–1379.

(7) Ong, S.; Zhao, X.; Eisenthal, K. B. Polarization of Water Molecules at a Charged Interface: Second Harmonic Studies of the Silica/Water Interface. *Chem. Phys. Lett.* **1992**, *191*, 327–335.

(8) Gonella, G.; Lütgebaucks, C.; de Beer, A. G. F.; Roke, S. Second Harmonic and Sum-Frequency Generation from Aqueous Interfaces Is Modulated by Interference. *J. Phys. Chem. C* **2016**, *120*, 9165–9173.

(9) Wen, Y.-C.; Zha, S.; Liu, X.; Yang, S.; Guo, P.; Shi, G.; Fang, H.; Shen, Y. R.; Tian, C. Unveiling Microscopic Structures of Charged Water Interfaces by Surface-Specific Vibrational Spectroscopy. *Phys. Rev. Lett.* **2016**, *116*, 016101.

(10) de Beer, A. G. F.; Campen, R. K.; Roke, S. Separating Surface Structure and Surface Charge with Second-Harmonic and Sum-Frequency Scattering. *Phys. Rev. B* **2010**, *82*, 235431.

(11) Jena, K. C.; Covert, P. A.; Hore, D. K. The Effect of Salt on the Water Structure at a Charged Solid Surface: Differentiating Second- and Third-Order Nonlinear Contributions. *J. Phys. Chem. Lett.* **2011**, *2*, 1056–1061.

(12) Rehl, B.; Rashwan, M.; DeWalt-Kerian, E. L.; Jarisz, T.; Darlington, A.; Hore, D. K.; Gibbs, J. M. New Insights into $\chi^{(3)}$ Measurements: Comparing Nonresonant Second Harmonic Generation and Resonant Sum Frequency Generation at the Silica/Aqueous Electrolyte Interface. *J. Phys. Chem. C* **2019**, *123*, 10991–11000.

(13) García Rey, N.; Weißenborn, E.; Schulze-Zachau, F.; Gochev, G.; Braunschweig, B. Quantifying Double-Layer Potentials at Liquid–Gas Interfaces from Vibrational Sum-Frequency Generation. *J. Phys. Chem. C* **2019**, *123*, 1279–1286.

(14) Ohno, P. E.; Wang, H.-f.; Geiger, F. M. Second-order Spectral Lineshapes from Charged Interfaces. *Nature Comm.* **2017**, *8*, 1032.

(15) Boamah, M. D.; Ohno, P. E.; Geiger, F. M.; Eisenthal, K. B. Relative Permittivity in the Electrical Double Layer from Nonlinear Optics. *J. Chem. Phys.* **2018**, *148*, 222808.

(16) Joutsuka, T.; Hirano, T.; Sprik, M.; Morita, A. Effects of Third-Order Susceptibility in Sum Frequency Generation Spectra: A Molecular Dynamics Study in Liquid Water. *Phys. Chem. Chem. Phys.* **2018**, *20*, 3040–5043.

(17) Joutsuka, T.; Morita, A. Electrolyte and Temperature Effects on Third-Order Susceptibility in Sum-Frequency Generation Spectroscopy of Aqueous Salt Solutions. *J. Phys. Chem. C* **2018**, *122*, 11407–11413.

(18) Pezzotti, S.; Galimberti, D. R.; Shen, Y. R.; Gaigeot, M.-P. What the Diffuse Layer (DL) Reveals in Non-Linear SFG Spectroscopy. *Minerals* **2018**, *8*, 305.

(19) Pezzotti, S.; Galimberti, D. R.; Shenb, Y. R.; Gaigeot, M.-P. Structural Definition of the BIL and DL: A New Universal Methodology to Rationalize Nonlinear $\chi^{(2)}(\omega)$ SFG Signals at Charged Interfaces, Including $\chi^{(3)}(\omega)$ Contributions. *Phys. Chem. Chem. Phys.* **2018**, *20*, 5190–5199.

(20) Wei, X.; Hong, S.-C.; Lvovsky, A. I.; Held, H.; Shen, Y. R. Evaluation of surface vs bulk contributions in sum-frequency vibrational spectroscopy using reflection and transmission geometries. *J. Phys. Chem. B* **2000**, *104*, 3349–3354.

(21) Ohno, P. E.; Chang, H.; Spencer, A. P.; Liu, Y.; Boamah, M. D.; Wang, H.-f.; Geiger, F. M. Beyond the Gouy–Chapman Model with Heterodyne-Detected Second Harmonic Generation. *J. Phys. Chem. Lett.* **2019**, *10*, 2328–2334.

(22) Ohno, P. E.; Wang, H.-F.; Paesani, F.; Skinner, J. L.; Geiger, F. M. Second-Order Vibrational Lineshapes from the Air/Water Interface. *J. Phys. Chem. A* **2018**, *122*, 4457–4464.

(23) Ohno, P. E.; Saslow, S. A.; Wang, H.-f.; Geiger, F. M.; Eisenthal, K. B. Phase-Referenced Nonlinear Spectroscopy of the α-Quartz/Water Interface. *Nature Comm.* **2016**, *7*, 13587.

(24) Tyrode, E.; Corkery, R. Charging of Carboxylic Acid Monolayers with Monovalent Ions at Low

Ionic Strengths: Molecular Insight Revealed by Vibrational Sum Frequency Spectroscopy. *J. Phys. Chem. C* **2018**, *122*, 28775–28786.

(25) Löbau, J.; Wolfrum, K. Sum-Frequency Spectroscopy in Total Internal Reflection Geometry: Signal Enhancement and Access to Molecular Properties. *J. Opt. Soc. Am. B* **1997**, *14*, 2505–2512.

(26) York, R. L.; Li, Y.; Holinga, G. J.; Somorjai, G. A. Sum Frequency Generation Vibrational Spectra: The Influence of Experimental Geometry for an Absorptive Medium or Media. *J. Phys. Chem. A* **2009**, *113*, 2768–2774.

(27) Liljeblad, J. F. D.; Tyrode, E. Vibrational Sum Frequency Spectroscopy Studies at Solid/Liquid Interfaces: Influence of the Experimental Geometry in the Spectral Shape and Enhancement. *J. Phys. Chem. C* **2012**, *116*, 22893–22903.

(28) Dalstein, L.; Potapova, E.; Tyrode, E. The Elusive Silica/Water Interface: Isolated Silanols Under Water as Revealed by Vibrational Sum Frequency Spectroscopy. *Phys. Chem. Chem. Phys.* **2017**, *19*, 10343–10349.

(29) Raybaut, M.; Godard, A.; Lubin, C.; Haidar, R.; Rosencher, E. Fresnel Phase Matching: A Universal Phase Matching Scheme. *C. R. Physique* **2007**, *8*, 1205–1212.

(30) Raybaut, M.; Godard, A.; Toulouse, A.; Lubin, C.; Rosencher, E. Fresnel Phase Matching: Exploring the Frontiers Between Ray and Guided Wave Quadratic Nonlinear Optics. *Opt. Exp.* **2008**, *16*, 18457–18478.

(31) Medhi, B.; Deb, S. Analytical Study of Broadband Second Harmonic Generation by Total Internal Reflection-Quasi Phase Matching Using the Concept of Highly Multimodal Nonlinear Guided Wave Approach in a Tapered Isotropic Slab of Zinc Telluride Crystal. *Optik* **2017**, *135*, 426–433.

(32) Avrutsky, I.; Soref, R. Phase-matched Sum Frequency Generation in Strained Silicon Waveguides Using Their Second-order Nonlinear Optical Susceptibility. *Opt. Express* **2011**, *19*, 21707–21716.

(33) Marowsky, G.; Canto-Said, E. J.; Lehmann, S.; Sieverdes, F. Phase-Matched Second-Harmonic Generation in Planar Waveguides. *Phys. Rev. B* **1993**, *48*, 18114–18118.

(34) Komine, H.; Long, W. H.; Tully, J. W.; Stappaerts, E. A. Quasi-Phase-Matched Second-Harmonic Generation by Use of a Total-Internal-Reflection Phase Shift in Gallium Arsenide and Zinc Selenide Plates. *Opt. Lett.* **1998**, *23*, 661–663.

(35) Bäumner, R.; Bonacina, L.; Enderlein, J.; Extermann, J.; Fricke-Begemann1, T.; Marowsky, G.; Wolf, J.-P. Evanescent-Field-Induced Second Harmonic Generation by Noncentrosymmetric Nanoparticles. *Opt. Express* **2010**, *18*, 23218–23225.

(36) Bey, P. P.; Giuliani, J. F.; Rabin, H. Nonlinear Reflection from a Phase-Matched Liquid near the Critical Angle. *Phys. Rev.* **1969**, *184*, 849–858.

(37) Conboy, J. C.; Daschbach, J. L.; Richmond, G. L. Total Internal Reflection Second-Harmonic Generation: Probing the Alkane Water Interface. *Appl. Phys. A* **1994**, *59*, 623–629.

(38) Fujiwara, K.; Monjushiro, H.; Watarai, H. Total Internal Reflection Second Harmonic Generation Spectrometer System Optimized for the Liquid/Liquid Interface. *Rev. Sci. Instrum.* **2005**, *76*, 023111.

(39) Schaefer, J.; Gonella, G.; Bonn, M.; Backus, E. H. G. Surface-Specific Vibrational Spectroscopy of the Water/Silica Interface: Screening and Interference. *Phys. Chem. Chem. Phys.* **2017**, *19*, 16875–16880.

(40) Dmitriev, V. G.; Gurzadyan, G. G.; Nikogosyan, D. N. *Handbook of Nonlinear Optical Crystals*, 3rd ed.; Springer-Verlag: Berlin, 1999.

(41) Darlington, A. M.; Gibbs-Davis, J. M. Bimodal or Trimodal? The Influence of Starting pH on Site Identity and Distribution at the Low Salt Aqueous/Silica Interface. *J. Phys. Chem. C* **2015**, *119*, 16560–16567.

(42) Leung, K.; Nielsen, I. M. B.; Criscenti, L. Elucidating the Bimodal Acid-Base Behavior of the Water-Silica Interface from First Principles. *Geochim. Cosmochim. Acta* **2010**, *74*, A584.

(43) Pfeiffer-Laplaud, M.; Costa, D.; Tielens, F.; Gaigeot, M.-P.; Sulpizi, M. Bimodal Acidity at the Amorphous Silica/Water Interface. *J. Phys. Chem. C* **2015**, *119*, 27354–27362.

(44) Sovago, M.; Campen, R. K.; Bakker, H. J.; Bonn, M. Hydrogen Bonding Strength of Interfacial Water Determined with Surface Sum-Frequency Generation. *Chem. Phys. Lett.* **2009**, *470*, 7–12.

(45) Ostroverkhov, V.; Waychunas, G. A.; Shen, Y. R. New Information on Water Interfacial Structure Revealed by Phase-Sensitive Surface Spectroscopy. *Phys. Rev. Lett.* **2005**, *94*, 046102.

(46) Myalitsin, A.; Urashima, S.-h.; Nihonyanagi, S.; Yamaguchi, S.; Tahara, T. Water Structure at the Buried Silica/Aqueous Interface Studied by Heterodyne-Detected Vibrational Sum-Frequency Generation. *J. Phys. Chem. C* **2016**, *120*, 9357–9363.

(47) Jena, K. C.; Hore, D. K. Variation of Ionic Strength Reveals the Interfacial Water Structure at a Charged Mineral Surface. *J. Phys. Chem. C* **2009**, *113*, 15364–15372.

(48) Urashima, S.-h.; Myalitsin, A.; Nihonyanagi, S.; Tahara, T. The Topmost Water Structure at a Charged Silica/Aqueous Interface Revealed by Heterodyne-Detected Vibrational Sum Frequency Generation Spectroscopy. *J. Phys. Chem. Lett.* **2018**, *9*, 4109–4114.

(49) Cyran, J. D.; Donovan, M. A.; Vollmer, D.; Siro Brigiano, F.; Pezzotti, S.; Galimberti, D. R.; Gaigeot, M.-P.; Bonn, M.; Backus, E. H. G. Molecular Hydrophobicity at a Macroscopically Hydrophilic Surface. *Proc. Nat. Acad. Sci. USA* **2019**, *116*, 1520–1525.

(50) Zhuravlev, L. T. The Surface Chemistry of Amorphous Silica. Zhuravlev Model. *Coll. Surf. A: Phys. Eng. Asp.* **2000**, *173*, 1–38.

(51) Brown, M. A.; Goel, A.; Abbas, Z. Effect of Electrolyte Concentration on the Stern Layer Thickness at a Charged Interface. *Angew. Chem. Int. Ed.* **55**, *2016*, 3790–3794.

Graphical TOC Entry